Composition-structure-property relationships of polyethylene vitrimers crosslinked by 8-arm polyhedral oligomeric silsesquioxane

Journal:	*Soft Matter*
Manuscript ID	SM-ART-12-2024-001518.R1
Article Type:	Paper
Date Submitted by the Author:	25-Feb-2025
Complete List of Authors:	Sadri, Mikaela; University of Southern Mississippi, School of Polymer Science and Engineering Barbour, Andrew; University of Southern Mississippi, School of Polymer Science and Engineering Thornell, Travis; US Army Corps of Engineers Waterways Experiment Station, Geotechnical and Structures Laboratory Newman, John; US Army, Engineering Research & Development Center Qiang, Zhe; University of Southern Mississippi, School of Polymer Science and Engineering

Composition-structure-property relationships of polyethylene vitrimers crosslinked by 8-arm polyhedral oligomeric silsesquioxane

Mikaela Sadri[1], Andrew Barbour[1], Travis L. Thornell[2], J. Kent Newman[2], Zhe Qiang[1]*

[1]School of Polymer Science and Engineering, The University of Southern Mississippi, Hattiesburg, MS, 39406
[2]U. S. Army Engineer Research and Development Center, Geotechnical and Structures Laboratory, Vicksburg, MS 39180
Correspondence to: Z. Q. (Email: zhe.qiang@usm.edu)

Abstract

Transforming polyolefins (POs), such as polyethylene (PE), into vitrimers is a promising research field due to their low cost, high availability, and excellent chemical resistance and mechanical properties. In these systems, the introduction of dynamic crosslinking can affect the degree of crystallinity in POs and may lead to phase separation due to incompatibility between the PO matrix and crosslinking agents, both of which can impact mechanical performance. This study investigates the relationship between crystallinity, crosslinking, and thermal-mechanical properties in commodity PE-derived vitrimers utilizing reactive 8-arm polyhedral oligomeric silsesquioxane (POSS) nanoparticles by deconvoluting the crosslinked and non-crosslinked components. Specifically, the insoluble crosslinked components displayed a lower modulus and increased brittleness, while the non-crosslinked phase performed similarly to neat PE. Together, the PE-vitrimer, crosslinked with 8-arm POSS, exhibited reduced toughness, elongation at break, and a slight increase in ultimate tensile strength. These behaviors were consistent when comparing the crosslinking density and gel fraction with a bifunctional crosslinker analogue. This work demonstrates the influence of nanoparticle-based crosslinker content on the mechanical properties of semi-crystalline PO-vitrimers, elucidating the roles of network density and crystallinity in determining their performance.

1. Introduction

Vitrimers are known as associate covalent adaptable networks (CANs), which consist of chemical crosslinks that are stable at service temperatures, but can become dynamic at elevated temperatures.[1] A key feature of vitrimers is their ability to undergo network rearrangement, resulting in reduced viscosity and faster relaxation times while maintaining a constant degree of crosslinking.[2–5] The dynamic nature of vitrimers allows for effective reprocessing and recycling of these chemically crosslinked materials, opening the door for improved sustainability within the field of polymer networks.[6–9] In 2017, Rottger et al.[10] reported a polyolefin (PO)-derived vitrimer, where dioxaborolane metathesis was used to convert polymers to vitrimers through post-functionalization. It was shown that the dynamically crosslinked materials could be reprocessed and maintain constant mechanical properties upon recycling three additional times while achieving improved dimensional stability at elevated temperatures. Since then, PO-derived vitrimers have garnered significant research interest due to the ubiquity and low cost of many commodity POs.

These materials involve a range of different dynamic crosslinking chemistries including dioxaborolane metathesis,[10–12] thiol-anhydride,[13] disulfide crosslinking,[14,15] silyl ether exchange,[16–19] imine exchange,[20–22] and transesterification.[23,24] The resulting studies have shown the conversion of commodity PO linear chains to vitrimers, which often resulted in changes in their crystallinity and mechanical properties. For these semi-crystalline POs, it has been observed that the degree of crystallinity as well as the size of the crystal spherulites and lamellae within systems is directly related to the thermal and mechanical properties within materials; specifically, crosslinking can reduce their degree of crystallization by limiting polymer chain mobility.

Notably, both crystallinity and crosslinking in PO-vitrimers significantly influence their mechanical performance, creating an intriguing interplay between these potentially competing effects. PO-based materials also often exhibit very limited compatibility with crosslinking agents, which can pose challenges in achieving homogeneous networks. In 2019, Ricarte et al.[11] reported phase separation of PE vitrimers due to the incompatibility between the PE backbone and the grafted dioxaborolane maleimide crosslinker moiety. Despite the observed phase separation, many of the reported PO-vitrimers appear to have comparable or even improved material properties.[10,16,24–26] In particular, the multi-phase systems have demonstrated the ability to influence the vitrimer properties as a result of both the crosslinked gel and non-crosslinked soluble fractions. Interestingly, in the field of polymer networks, using multi-arm crosslinkers to increase the number of reactive sites can improve the crosslinking density, leading to denser networks up to a certain limit.[27–30] However, to date, typical crosslinking agents for preparing PE-derived vitrimers have been limited to bifunctional molecules. As a result, the use of multi-arm crosslinkers in PE-derived vitrimers remains underexplored, particularly since their potential to modulate network formation and crosslinking density, as well as disrupt crystalline regions, could significantly impact mechanical properties. The conversion of commodity POs into dynamic networks crosslinked using multi-arm nanoparticles creates new opportunities for physical studies on intriguing material properties within these complex semi-crystalline dynamic network systems.

This study utilizes 8-arm polyhedral oligomeric silsesquioxane (POSS) nanoparticles as dynamic crosslinkers to prepare PE-derived vitrimers, focusing on understanding the impact of crosslinker content on morphology and properties; their properties are also compared with physically blended samples containing non-reactive POSS. It is noted that while POSS is prevalent within nanocomposite research for potential improvements in thermal stability, oxidative resistance, and polymer processing,[31–36] the use of these multifunctional nanoparticle-based crosslinkers for the formation of PO-vitrimers has not been previously reported. Specifically, this work separately analyzed the soluble and insoluble fractions of PE-derived vitrimers to further explore the interplay between crosslinking and crystallinity on the thermal and mechanical properties of the vitrimer components. It is found that the multi-component PE vitrimers, formed through dynamic crosslinking with 8-arm POSS, exhibit increased strength and decreased stretchability due to the network formation. However, the elastic modulus decreases as a result of the lowered crystallinity. This work provides important insights into the role of crosslinking in PO vitrimers and the tradeoffs between network density and crystallinity.

2. Experimental

2.1. Materials. TYMAX® maleated linear low-density PE, grade GT4300 [PE_{neat}, maleic anhydride (MA) content: ~1.5 wt.% determined by titration] was manufactured by Westlake Chemical. Glycidyl polyhedral oligomeric silsesquioxane, (GPOSS) cage mixtures and OctaIsobutyl POSS® (OIbPOSS) were purchased from Hybrid Plastics. Zinc stearate (ZnSt) and bisphenol A diglycidyl ether (DGEBA) were obtained from Sigma-Aldrich. Xylene (99 %) and methanol were purchased from Thermo Scientific. All chemicals were used as received unless noted otherwise.

2.2. Sample Preparation. PE-GPOSS vitrimers, PE-DGEBA vitrimers, and PE-OIbPOSS physical blends were compounded by an Xplore MC5 microcompounder at 200 °C using a screw speed of 20 rpm unless otherwise noted. In typical vitrimer formulations, mixtures of PE_{neat} (2.9 g) and ZnSt (1 wt.% of the PE_{neat} amount) were introduced into the microcompounder together. After the first half of the PE/ZnSt mixture was loaded, the POSS or DGEBA was added into the compounder using a syringe, followed by the rest of the PE/ZnSt mixture. In blend formulations, mixtures of PE_{neat} and OIbPOSS were introduced to the compounder together. For all sample preparations, the GPOSS and OIbPOSS content was added at controlled molar ratios of POSS functional groups (PFGs) to MA content, as described in Table 1. Recirculation time for all formulations was 5 min, determined from the force output which corresponds to the viscosity of the compounded materials. The screw speed and recirculation time used in this study were optimized by a series of experiments on how shear rate and shear time processing influence derived materials properties, to ensure proper mixing without overprocessing of the materials. These results are shown in Figures S1-S6. When reprocessing the insoluble fractions of the PE-vitrimers, 1 wt.% of ZnSt was added back into the system to allow for continued dynamic exchange and better processing (Figure S7), as it was removed upon the gel extraction step.

Table 1. Material compositions of PE vitrimers (PE_v) and PE blends (PE_b).

Name	Formulation	POSS type	[PFG]/[MA]	POSS content (wt.%)	POSS content (vol.%)
PE_v-0.5	Vitrimer	GPOSS	0.5	1.3	0.9
PE_v-1.0	Vitrimer	GPOSS	1.0	2.5	1.8
PE_v-1.5	Vitrimer	GPOSS	1.5	3.7	2.7
PE_v-2.0	Vitrimer	GPOSS	2.0	4.9	3.6
PE_v-3.0	Vitrimer	GPOSS	3.0	7.1	5.3
PE_b-0.5	Blend	OIbPOSS	0.5	0.8	0.7
PE_b-1.0	Blend	OIbPOSS	1.0	1.6	1.3
PE_b-1.5	Blend	OIbPOSS	1.5	2.4	2.0
PE_b-2.0	Blend	OIbPOSS	2.0	3.2	2.6
PE_b-3.0	Blend	OIbPOSS	3.0	4.8	3.9

2.3. Material characterization. The MA content was determined by titration using a previously reported procedure.[25] The gel fraction of the vitrimer networks was determined via an extraction method. Specifically, PE_v were submerged in hot xylenes (120 °C) for 24 h, after which the soluble and insoluble fractions (referred to as $PE_{v\text{-sol}}$ and $PE_{v\text{-insol}}$, respectively) were separated. The $PE_{v\text{-sol}}$ was precipitated into cold methanol and separated through gravity filtration. The $PE_{v\text{-sol}}$ and remaining $PE_{v\text{-insol}}$ were then both dried under vacuum at 60 °C for 24 h. The gel fraction was calculated via the following equation:

$$gel\ fraction = \left(\frac{w_f}{w_i}\right) \times 100\% \tag{1}$$

where w_i and w_f are the masses of the PE_v before and the $PE_{v\text{-insol}}$ after gel extraction, respectively. Fourier transfer infrared (FTIR) spectroscopy was performed on all samples using a PerkinElmer Frontier FTIR-IR spectrometer with the universal attenuated total reflectance (ATR) sampling accessory attached. An average of 32 scans were taken, each with a resolution of 4 cm^{-1} from 4000 to 600 cm^{-1}.

The thermal stability of each sample was determined by thermogravimetric analysis (TGA) using a thermogravimetric analyzer Q50 (TA Instruments), where samples were heated under nitrogen atmosphere at 10 °C/min up to 600 °C. The temperature at which 5 % mass loss occurred (T_{d5}) was recorded. Differential scanning calorimetry (DSC) using a TA Instruments Discovery DSC250 was performed to characterize the melting and crystallization temperatures (T_m and T_c, respectively) as well as the degree of crystallinity (X_c). Each sample underwent a heat-cool-heat cycle from -90 to 250 °C at a ramp rate of 10 °C/min using aluminum sample pans. T_c and T_m were determined by the temperature at the peak heat flow from the cooling and second heating step, respectively. χ_c was calculated via the following equation:

$$\chi_c = \left(\frac{\Delta H_f}{\Delta H_f^0}\right) \times 100\% \tag{2}$$

where ΔH_f is the enthalpy of fusion and $\Delta H_f^0 = 293$ J/g is the standard enthalpy of fusion for PE.

Crystal lamellar thickness (L) and the lamellar thickness distributions were also characterized through DSC measurements, where the Gibbs-Thomson equation (equation 3) was used for L and equation 4 describes the thickness distributions.

$$T_m = T_m^0\left(1 - \frac{2\sigma_e}{\Delta H_{f,c}^0 L}\right) \tag{3}$$

$$\frac{1}{M}\frac{dM}{dL} = \frac{dE}{dT}\frac{(T_m^0 - T_m)^2 \rho_c}{2\sigma_e T_m} \tag{4}$$

where T_m is the observed melting temperature (unit: K) for a crystalline lamella of thickness L, T_m^0 is the equilibrium melting temperature of PE (415 K), $\Delta H_{f,c}^0$ is the enthalpy of fusion for the crystalline phase (288 J/cm^3), and σ_e is the surface energy of the basal surface of a lamellar crystal (6.09x10^{-6} J/cm^2). Additionally, M is the mass of the crystalline phase within the sample, dE/dT is the energy required for melting the dM portion of the crystalline phase (the heat flow from DSC), and ρ_c is the density of the crystal phase (~1 g/cm^3). TGA and DSC data acquisition and analysis were performed using TRIOS software (TA Instruments).

Tensile testing and dynamic mechanical analysis (DMA) specimens (2 cm x 0.5 cm x 0.05 cm) were prepared using a Carver 4386 press where samples were pressed at 165 °C for a total of 15

min (10 min heating with no pressure, 3 min under 3 metric tons, and 2 min under 6 metric tons) using polytetrafluoroethylene (PTFE) release film above and below the mold, before cooling on an aluminum bench with a steel heat sink on top, holding the mold together for 20 min until removing cooled specimens. Uniaxial extension tests of PE materials were performed on a Mark-10 F105-EM test frame equipped with a series FS05-50 force sensor with a 250 N capacity at a strain rate of 10 mm/min. Igor Pro 9.05 was used for data analysis, where ultimate tensile strength (UTS) was determined by the maximum tensile stress achieved prior to sample failure, Young's modulus was calculated as the slope of the linear region of the curve before yield, and toughness was determined by integrating the stress-strain curves for each sample. DMA tests were performed via a Discovery DMA 850 (TA Instruments), where vitrimer specimens underwent a temperature ramp from 40 to 220 °C at a heating rate of 2 °C/min at a frequency of 0.01 % strain in tensile mode using a film tension clamp fixture.

Polarized optical microscopy (POM) (Olympus BX53M) equipped with a temperature controller (Linkam LTS-420) was used to characterize the crystalline morphology of the PE materials. Polarized images were taken by an Olympus DP28 camera in transmission mode, at 90° angle configuration between the linear polarizer and linear analyzer. Samples were heated from room temperature to 200 °C, held for 5 min, then cooled to below 100 °C, all at ramp rate of 50 °C/min).

3. Results and Discussion

Figure 1a shows the chemical structures of key components used in this study, where maleic anhydride functionalized PE (PE_{neat}) was converted into PE-derived vitrimers (PE_v) via crosslinking with epoxide-functionalized glycidyl POSS (GPOSS) through a ring-opening reaction. The resulting ester crosslinkers are thermally reversible with the presence of ZnSt catalyst, as illustrated in Figure 1b, enabling the dynamic nature of the PE-derived network at elevated temperatures. Additionally, blends of PE_{neat} and unfunctionalized OIbPOSS (PE_b) at varied molar ratio were prepared, allowing us to study the roles of the nanoparticle additive and dynamic crosslinking on material properties. In this work, a variety of samples were prepared using different molar ratios of PFG to grafted MA on PE, including 0.5, 1.0, 1.5, 2.0, and 3.0.
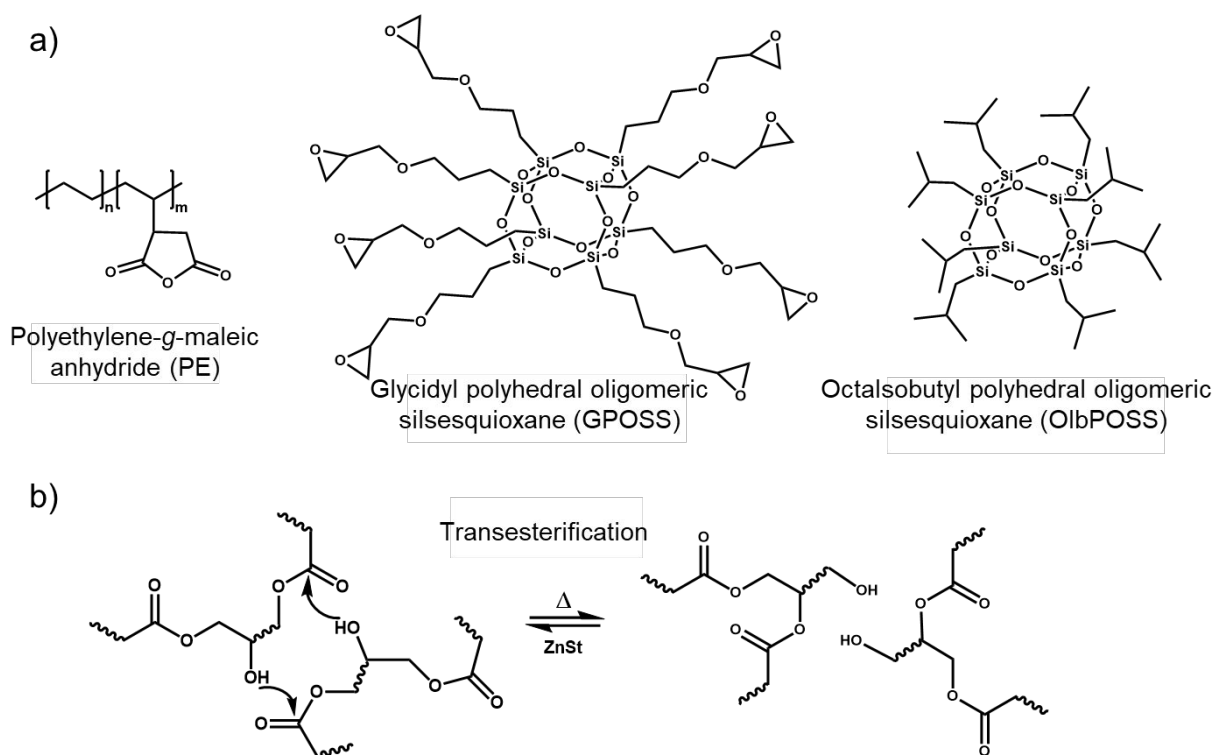
Figure 1. Chemical structures (a) of PE, GPOSS, and OIbPOSS used for PE$_v$ and PE$_b$ materials. (b) an illustration of dynamic transesterification of the PE$_v$ materials.

FTIR was used to confirm the crosslinking reaction between epoxy-anhydride groups from the synthesis of PE$_v$. As shown in Figure 2a, the PE$_{neat}$ sample displays the alkane stretching bands at 2918 and 2850 cm^{-1} and bending band at 1470 cm^{-1}. Additionally, the band at 718 cm^{-1} corresponds to CH$_2$ rocking. These bands can also be observed in all PE$_v$ samples, with constant relative absorbance levels to each other. However, as the POSS loading level increases, another band begins to emerge at 1110 cm^{-1}, which is associated with the Si-O bond stretching from the POSS cages (Figure S8), showing a clear increase with a higher loading content of GPOSS in vitrimers. Figure 2b confirms the epoxy-anhydride curing in PE$_v$. Unlike with the addition of OIbPOSS in PE$_b$ samples (Figure S9), as the GPOSS content increases, the intensity of MA-related bands at 1715 and 1780 cm^{-1} decrease (Figure S10), while simultaneously another band emerged at 1730 cm^{-1}, corresponding to the reaction of MA into forming ester groups.[37,38] Solvent extraction experiments were performed to understand how gel content in derived vitrimers was impacted by POSS loading levels (Figure 2c). While PE$_{neat}$ and PE$_b$ were completely dissolved throughout these tests, an insoluble fraction (PE$_{v-insol}$) can be found in all PE$_v$ samples. With increasing molar ratio of GPOSS, there was a corresponding increase in gel fraction. For PE$_v$-0.5, the gel content was 51.2 wt.% which increased to 55.1 and 68.8 wt.% for PE$_v$-1.0 and PE$_v$-3.0, respectively. This gradual increase is consistent with FTIR results, confirming the increased formation of crosslinking from higher GPOSS loadings. However, it is important to note that GPOSS

crosslinker contains eight epoxide groups, of which a minimum of two are required to form crosslinking sites via reacting with MA groups from PE backbones. As a result, many of the epoxide groups can remain unreacted.
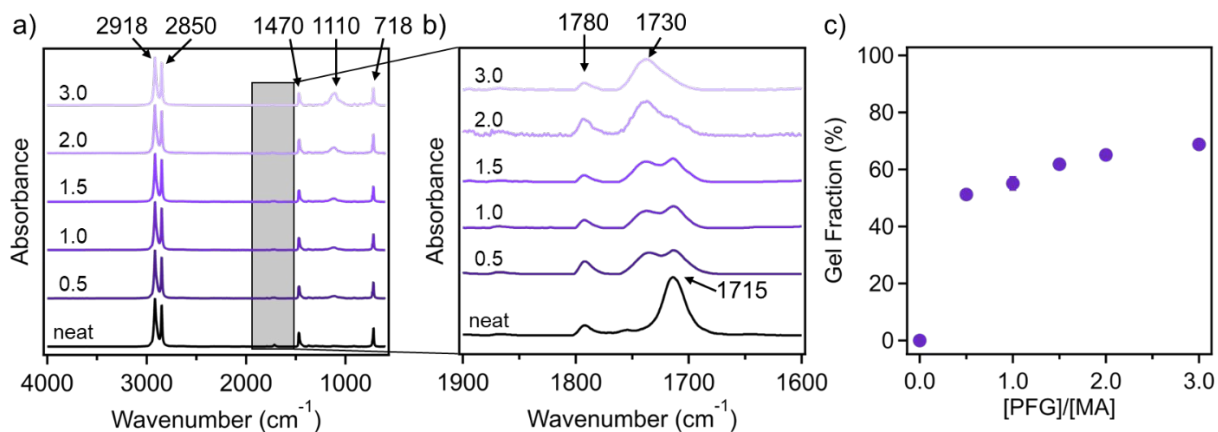

Figure 2. (a) FTIR spectra of PE_{neat} and PE_v with varying molar ratios of PFG to MA using GPOSS, where (b) shows a closeup range of the bands corresponding to the epoxy-anhydride reactions. (c) Gel fraction as a function of [PFG]/[MA] molar ratios, determined by gel extraction in hot xylenes, where error bars are included in the symbols yet too small to see.

TGA was used to determine thermal stability of the PE_v materials, as shown in Figure 3. It was found that all PE_v samples have a lower T_{d5} than neat PE. Specifically, T_{d5} for PE_{neat} is 457.5 °C, and exhibits a decrease upon increasing GPOSS loading content, from 450.8 °C for PE_v-0.5 to 436.3 °C for PE_v-3.0. In the control PE_b samples, a larger reduction in T_{d5} from 457.5 °C for PE_b-0.5 to 417.7 °C for PE_b-3.0 was observed (Figure S11a). The difference in thermal stability with increasing POSS content is likely because POSS molecules are less thermally stable than PE chains (T_{d5} for GPOSS: 395 °C and T_{d5} for OIbPOSS: 237 °C, Figure S11b). Additionally, the network was formed through the creation of ester bonds, and the observed change in thermal stability upon vitrimer formation likely stems from the inherent thermal susceptibility of ester bonds.
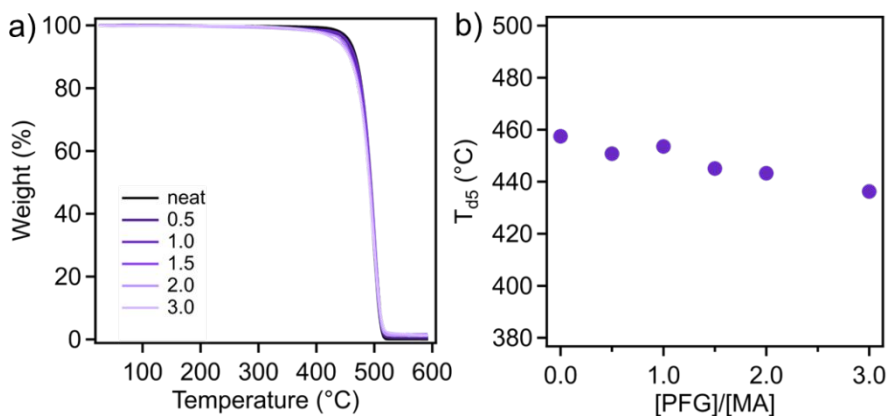

Figure 3. (a) TGA curves for PE_{neat} and PE_v samples heated at 10 °C/min and (b) the corresponding T_{d5} values.

7

DSC was performed to understand the impact of dynamic crosslinking on the crystallization and melting behaviors of the PE_v materials. Figure 4a and Figure 4b show one clearly identifiable feature, corresponding to the crystallization and melting events, respectively. The crystallization exotherm and melting endotherm of PE_{neat} have a single peak, located at 106.6 °C and 121.9 °C respectively, suggesting a single main crystallite size population. All PE_v samples showed clear bimodal behavior, indicative of two different crystallite size populations. The two different melting temperatures will be referred to as $T_{m,low}$ and $T_{m, high}$, in order to distinguish between the higher and lower melting temperatures. There are two things to note: the first is that $T_{m,high}$ for each PE_v is very similar to T_m for PE_{neat}, as shown in Table S1 with less than 0.5 °C difference. Secondly, the relative peak size and dominance appears to shift from $T_{m,high}$ to a higher level of $T_{m,low}$ as the POSS loading content increases. Alternatively, the PE_b samples had one distinct melting and crystallization peak across all ratios (Figure S12), changing by less than 1.5 °C for T_m of PE_b-0.5 to PE_b-3.0, and less than 1 °C for T_c of PE_b-0.5 to PE_b-3.0, corresponding closely with PE_{neat} values. These results suggest the presence of two mixed components within PE_v samples, which can be contributed to crosslinked and uncrosslinked phases. Interestingly, despite differences in gel fraction and GPOSS loading content in the PE_v samples, the crystallinity corresponding to the PE weight percentage remained relatively stable, changing only slightly within the range of 45% to 49%.
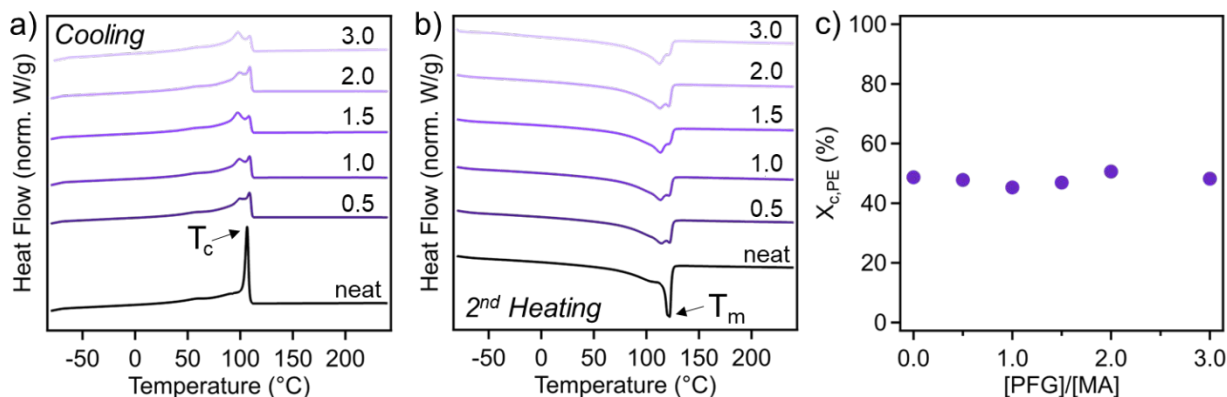

Figure 4. DSC thermograms of the (a) cooling and (b) second heating steps showing the T_c and T_m, respectively, for PE_{neat} and PE_v samples. (c) The degree of crystallinity normalized by the weight percent PE ($\chi_{c,PE}$) within each material.

To fully understand the emergence of the two distinct crystallite sizes observed in the bimodal DSC peaks, PE_v materials were separated into soluble and insoluble components, which were then isolated and studied. This was performed via gel extraction, where the $PE_{v\text{-insol}}$ is the insoluble (or gel) fraction, and $PE_{v\text{-sol}}$ is the soluble fraction that was then precipitated out and dried. DSC was then performed on the separated $PE_{v\text{-insol}}$ and $PE_{v\text{-sol}}$ components, where Figure S13 shows the DSC thermograms of each component upon cooling and heating. Through these thermograms it can be observed that unlike the PE_v samples, each crystallization and melting peak is unimodal, showing a single majority crystallite size population. Furthermore, while each component shows a single

crystallizing exotherm or melting endotherm, there is a clear distinction between T_c and T_m for PE_{v-sol} and $PE_{v-insol}$. These temperature differences correspond directly with the bimodal peaks found within the bulk PE_v, further suggesting that the PE_v have two distinct phases between the crosslinked PE and the linear PE within the same system, when using GPOSS nanoparticles as crosslinkers.

The characteristic temperatures for each component remained consistent, even with increasing POSS content. For example, Figure 5a shows the T_c for $PE_{v-insol}$-0.5, $PE_{v-insol}$-1.0, $PE_{v-insol}$-1.5, $PE_{v-insol}$-2.0, and $PE_{v-insol}$-3.0 are 96.4, 96.6, 96.0, 95.9, and 96.1 °C, respectively, with a change of less than 1 °C among all samples. Similar consistency was also reported for PE_{v-sol}, where T_c for PE_{v-sol} samples 0.5, 1.0, 1.5, 2.0, and 3.0 were 104.4, 106.3, 102.9, 104.9, and 109.8 °C, respectively. The T_m difference for both $PE_{v-insol}$ and PE_{v-sol} were also less than 2 °C and 7 °C, as shown in Figure S13. These behaviors within each respective component continue to be illustrated by χ_c remaining relatively unchanged within each component (Figure 5b). There is a clear difference in χ_c between the PE_{v-sol} and $PE_{v-insol}$ components, which is due to crosslinks in the $PE_{v-insol}$ network limiting the ability of polymer chains to form crystals. However, similar to the characteristic crystallization/melting temperatures, the χ_c only changes by 2.1 and 3.7 % for $PE_{v-insol}$ and PE_{v-sol}, respectively when varying the POSS loading levels from 0.5 to 3.0. When normalizing the degree of crystallinity by PE content, the $\chi_{c,PE}$ is notably less for $PE_{v-insol}$ materials than for the PE_{v-sol} materials, averaging 40.4 % and 47.0 %, respectively (Table S1).

Furthermore, the distribution of crystallite lamella thicknesses (L) can be directly calculated from the DSC heating thermogram via equation 4. Figures 5c-d show these relative probability distributions of the crystallite lamellar thicknesses for bulk PE_v and the corresponding $PE_{v-insol}$ components. It can be found that PE_{neat} has a single population of L, ranging from ~8-9 nm. However, upon crosslinking, two distinct size populations appear, one at 6.4 nm, and another at 9.0 nm for PE_v-0.5. Each sample exhibits two distinct populations, which shift slightly with increasing POSS loading. At higher POSS contents, the populations shift by less than 0.5 nm, reaching 6.0 nm and 8.7 nm for PEv-3.0. Unlike the bimodal populations within PE_v, $PE_{v-insol}$ samples have one distinct L population, which is approximately 5.7 nm for all samples. The PE_{v-sol} materials also showed distinct unimodal L populations, as shown in Figure S14, where L is 7.0, 7.3, 6.4, 7.5, and 8.3 nm for PE_{v-sol}-0.5, PE_{v-sol}-1.0, PE_{v-sol}-1.5, PE_{v-sol}-2.0, and PE_{v-sol}-3.0, respectively. Separating different components within the PE_v allows for further understanding of the structure-property relationship within these semi-crystalline vitrimers. Specifically, it is found that the L for the $PE_{v-insol}$ materials is smaller due to crosslinking, which hinders the crystal formation. Decreased L and crystallinity have been previously noted in other PE-derived vitrimer systems, also attributed to network formation.[39,40] These behaviors explain the relationship between the PE_v and its composition impacts on L within the PE-POSS-derived vitrimers.
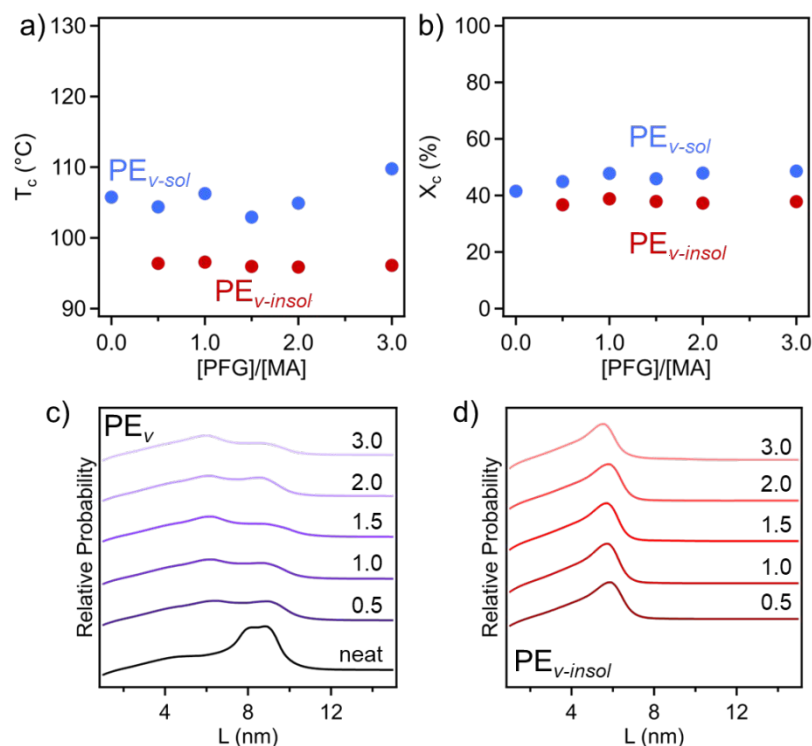
Figure 5. a) T_c and (b) χ_c of different PE$_{v\text{-sol}}$ (blue) and PE$_{v\text{-insol}}$ (red) samples from DSC. Lamellar thickness distribution for (c) PE$_v$ and (d) PE$_{v\text{-insol}}$.

The POM images in Figure 6 further demonstrate the differences in the semi-crystalline morphology of the material components, particularly in their spherulite formation. PE$_{neat}$, PE$_{v\text{-sol}}$, and PE$_b$ each show the distinctive Maltese cross as the PE phases crystallized upon cooling from 200 °C at 50 °C/min into large-size spherulites. Alternatively, while PE$_v$ does not show distinguishable spherulites, there are still clear brighter and darker regions, indicative of crystal formation within the lighter regions, where the individual spherulites are too small to be observed on this scale. This is likely a direct result of the crosslinking within PE$_v$, where both the crosslinking and the presence of POSS hinder the formation of large spherulites. These results are consistent with other PE-derived vitrimer research such as from Montoya-Ospina et al.[39] and Maaz et al.[41], where Maltese crosses were found in the spherulites for both the neat PE and PE-*g*-MA, but no distinct large spherulites within the crosslinked vitrimers. Furthermore, there are significant differences in the average spherulite sizes between each material with PE$_b$ being the smallest. These differences can be explained by the higher percentage of defect sites from both the grafted MA and the blended OIbPOSS content which disturbs the continuous spherulite. Within PE$_b$, the inclusion of the OIbPOSS can impact the continuous phase which decreases the spherulite size and potentially impedes growth, while still allowing for a similar degree of crystallization. Alternatively, PE$_{v\text{-sol}}$ appears to have a larger average spherulite size than PE$_{neat}$. This is likely a

result of less MA content within PE_{v-sol} upon the solvent extraction process as compared with the PE_{neat}; this allows for increased continuous PE phase spherulites due to a decrease in defect sites.
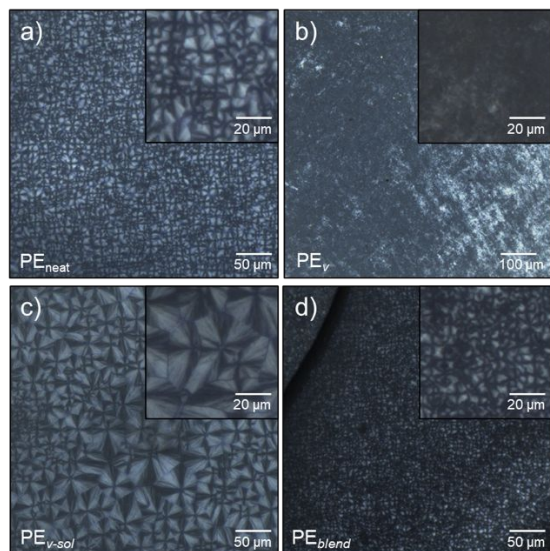

Figure 6. POM images at 100 °C after cooling from 200 °C at 50 °C/min of (a) PE_{neat}, (b) PE_v-1.0, (c) PE_{v-sol}-1.0, and PE_b-1.0

To understand the impact of POSS loading and crosslinking degree on the mechanical properties of the vitrimer, tensile tests were performed for both the PE_v and PE_b samples as shown in Figure 7. All measured parameters of the PE_b materials, including ultimate tensile strength (UTS), strain at break, and toughness, behaved similarly to the PE_{neat} material. For example, the UTS of PE_{neat} is 10.0 MPa, which becomes 10.1 MPa for PE_b-2.0 and 9.8 MPa for PE_b-3.0 (Figure S15). The strain at break and toughness of PE_{neat} are 669 % and 58.5 MJm^{-2}, while for PE_b-2.0 they are 659 % and 58.0 MJm^{-2}, and for PE_b-3.0 they are 635 % and 53.9 MJm^{-2}, respectively (Figure 7c-d). These results suggest that the inclusion of POSS nanoparticles in PE samples, without the formation of new chemical bonds, does not significantly impact the material properties. It is noted that the critical aggregation concentration of OIbPOSS in PE is 5 wt. %,[42,43] and the PE_b-3.0 materials have an OIbPOSS content of 4.8 wt.%. Therefore, it is assumed that the aggregation of POSS chemicals within the PE matrix in this study should be minimal, with most uniformly distributed throughout the material. Notably, conversion of PE_{neat} into PE_v has a very significant impact on their resulting mechanical properties. These distinct property changes can be described by a simultaneous increase in strength and decrease in stretchability. Specifically, PE_v materials exhibited a significant increase in ultimate tensile strength (UTS), increasing from 10.0 MPa (PE_{neat}) to 12.0 MPa (PE_v-0.5), as a result of crosslinking (Figure S15). Furthermore, the strain at break decreases from 669 % for PE_{neat} to 362, 337, 337, 399 and 351 % for PE_v-0.5, PE_v-1.0, PE_v-1.5, PE_v-2.0 and PE_v-3.0, respectively (Figure 7c). This decrease in strain is also attributed to the network formation, where an increased number of crosslinks reduces stretchability of a material by limiting its degrees of polymer chain freedom. Interestingly though, all PE-derived vitrimers also saw a notable decrease in the Young's modulus, from PE_{neat}: 119.4 MPa to PE_v-0.5:

100.9 MPa, PE$_v$-1.0: 100.0 MPa, PE$_v$-1.5: 98.8 MPa, PE$_v$-2.0: 103.9 MPa, and PE$_v$-3.0: 98.7 MPa. Similar decrease in elastic modulus has been reported before and is likely a result of the changed χ_c and crystalline structures in the PE$_v$ materials as compared with the PE$_{neat}$ and PE$_b$.[16] Specifically, the reduction in elastic modulus is attributed to the decreased crystallization in PE$_v$ samples due to network formation, which restricts chain mobility. In PO materials, it is well known that the degree of crystallinity plays a crucial role in controlling the elastic modulus of the samples, as the amorphous domains are often soft. Overall, despite crosslinking in PE$_v$ samples, the increase in strength does not compensate for the significant reduction in elongation, which in turn explains the decrease in toughness. Moreover, similar to the behavior observed within the gel fraction experiments, upon crosslinking at the 0.5 ratio, there was an immediate property change resulting from the initial network formation. However, upon higher GPOSS loading, PE$_v$ maintains a relatively consistent modulus, strain at break, and toughness.
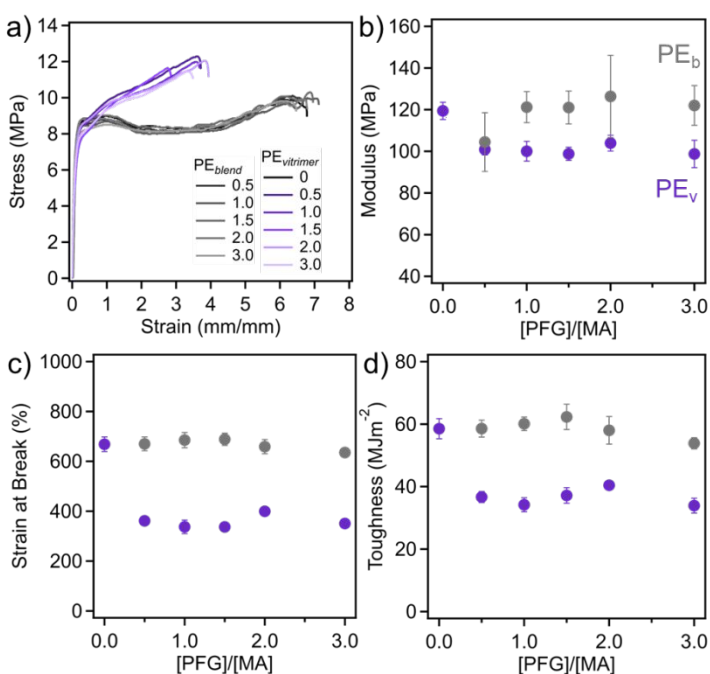

Figure 7. Mechanical properties of PE$_{neat}$ (black), PE$_v$ (purple), and PE$_b$ (gray) with varied POSS content, including (a) representative tensile curves, (b) Young's modulus, (c) strain at break, and (d) toughness.

Figure 8 shows key mechanical properties under tension for PE$_v$, PE$_{v-sol}$, and PE$_{v-insol}$, derived from PE$_v$-1.0 to further understand the impact of crosslinking on PE vitrimers. For nearly all evaluated properties PE$_v$ lies somewhere between PE$_{v-sol}$ and PE$_{v-insol}$, consistent with the nature of PE$_v$ containing two distinct phases. For instance, the modulus of PE$_v$ is 92.7 MPa, while PE$_{v-sol}$ is higher at 102.5 MPa and PE$_{v-insol}$ is lower at 84.2 MPa. The crosslinks within PE$_{v-insol}$ result in a lower degree of crystallinity, ultimately decreasing the material elastic modulus as compared with the uncrosslinked counterpart. Along with the modulus changes, the difference in the strain at break is also apparent between each sample. PE$_{v-sol}$ has a high strain at break of 548.2 %, with

strain softening and necking behavior after a distinctive yield, which can be found in their stress-strain curves as distinctive characteristics in semi-crystalline polymers due to the tilting of crystal lamella. Alternatively, both PE_v and $PE_{v\text{-insol}}$ exhibited significant strain hardening behavior directly after yield, a result of the crosslinked network having decreased lamellar thickness, where the onset of strain hardening corresponds to the complete transformation of the original lamellar structure into a microfibrillar morphology,[44] which leads to a more brittle material with a much lower ultimate strain (PE_v: 337.3 %, $PE_{v\text{-insol}}$: 190.0%). In addition, crosslinked samples displayed higher UTS than the $PE_{v\text{-sol}}$ fraction, from 8.3 MPa for $PE_{v\text{-sol}}$ to 11.1 MPa and 12.0 MPa for $PE_{v\text{-insol}}$ and PE_v, respectively. The interplay between decreased strain at break with a higher UTS leads to altered toughness upon varying GPOSS content, resulting in differences in overall toughness from 42.1 MJm^{-2} for $PE_{v\text{-sol}}$ and 17.6 MJm^{-2} for $PE_{v\text{-insol}}$. The lower yield stress observed in $PE_{v\text{-insol}}$ compared to PE_v may be attributed to the decreased crystallinity (χ_c), which results in reduced intermolecular bonding. The rest of the $PE_{v\text{-insol}}$ materials with varied GPOSS loading levels behave similarly to $PE_{v\text{-insol}}$-1.0 when compared with their PE_v counterpart, where the insoluble fraction has a lower modulus, toughness, strain at break, and UTS (Figure S16). The yielding and breaking behavior are also consistent, where a significant strain hardening behavior can be observed. These properties can be explained by differences in overall crosslinking content which decreases the material crystallinity and thereby lowers overall material stiffness and reduces chain mobility. Many of the trends observed within the $PE_{v\text{-insol}}$ materials mirror the trends observed in the PE_v samples. For example, many of the extracted mechanical properties appear to have one trend in behavior up until ~5 wt.%, where it then deviates, which can be attributed to potential agglomeration of the GPOSS, disrupting homogenous crosslink formation.
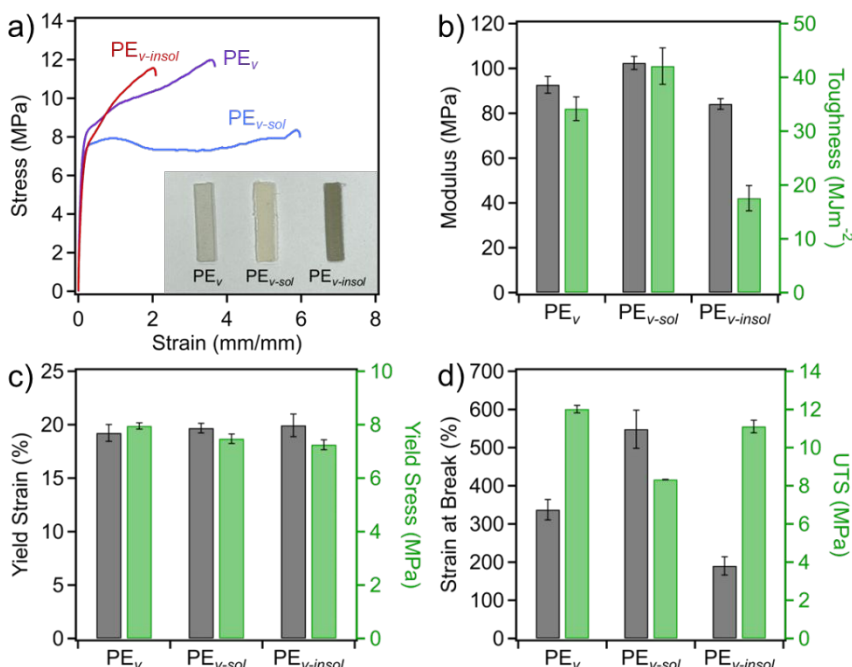
Figure 8. Mechanical properties of PE_v, PE_{v-sol}, and $PE_{v-insol}$ components for PE_v-1.0, where (a) are representative curves and photo of the melt pressed bars used for tensile testing. (b-d) are the extracted mechanical properties of each component.

In addition to understanding the mechanical properties at room temperature, DMA was utilized to investigate the storage modulus (E') and relative crosslinking behavior of PE_{neat}, PE_v, and $PE_{v-insol}$ materials at elevated temperatures. For vitrimer samples, the decreasing in their E' compared to pristine PE can be attributed to reduced crystallinity at temperatures below melting or glass transition,[45–47] which is consistent with the χ_c determined from DSC, where PE_{neat} has the highest E' at 50 °C of 170.8 MPa and also the largest χ_c at 48.7 % (Figure 9a). Upon crosslinking PE_v-0.5 has a decrease in E' with a simultaneous decrease in χ_c, to 147.0 MPa and 47.2 %, respectively. These properties are further decreased with increasing network formation, where E' and χ_c for PE_v-3.0 are 107.8 MPa and 44.8 %, respectively, which is also consistent with the trends observed with the elastic modulus from tensile experiments. Additionally, the melting behavior, distinguished by the characteristic drop in E', for PE_v materials appears to span across the T_m range of PE_{neat}, beginning before ($T_{m,onset}$) and ending after ($T_{m,endset}$) PE_{neat}. Specifically, $T_{m,onset}$ is 115 °C for PE_{neat} and ranges from 107 to 118 °C for all PE_v samples. $PE_{m,endset}$ cannot be determined for PE_{neat} by DMA due to the material flowing upon increased temperature, but ranges from 123 to 131 °C for all PE_v samples. This is consistent with the DSC bimodal T_m peaks found within the PE_v samples, where the $PE_{v-insol}$ component is responsible for the lower T_m, and the PE_{v-sol} component melts at a slightly higher temperature, and both components are present within each PE_v sample, explaining the range for $T_{m,onset}$ and $T_{m,endset}$. While all PE_v materials demonstrated a rubbery plateau above the melting pointing, indicating the formation of crosslinks, PE_{neat} continued to drop in E' until it flowed which prevented further measurements via the tension film setup. Relative E'

values of the rubbery plateau are associated with relative crosslinking density and network behaviors, where higher E' suggest that on average the molecular weight between crosslinks are smaller (a more densely formed polymer network). It is found that the plateau modulus measured at 150 °C for PE_v-0.5 is the lowest, at 0.5 MPa and PE_v-3.0 is the highest, at 1.1 MPa, with PE_v-1.0, PE_v-1.5, and PE_v-2.0 falling in between at 0.83, 0.82, and 1.0 MPa, respectively.

While the DMA behavior for PE_v samples demonstrated variability due to differing amounts of network formation, the $PE_{v\text{-insol}}$ materials are much more consistent (Figure 9b). The E' values at 50 °C for all $PE_{v\text{-insol}}$ samples are significantly lower than those of PE_{neat}, reflecting the much lower crystallinity in the insoluble fractions of the vitrimers. This reduction in crystallinity results in the materials being considerably less stiff than the neat PE. Specifically, E' at 50 °C for $PE_{v\text{-insol}}$-0.5, $PE_{v\text{-insol}}$-1.0, $PE_{v\text{-insol}}$-1.5, $PE_{v\text{-insol}}$-2.0, and $PE_{v\text{-insol}}$-3.0 is 89.2, 88.0, 91.8, 79.1, and 84.4 MPa, respectively. Moreover, the characteristic drop of E' within $PE_{v\text{-insol}}$ materials occurs at a lower temperature than PE_{neat}, consistent with the decrease in T_m according to DSC for all $PE_{v\text{-insol}}$ samples. $T_{m,onset}$ ranges from 100 to 102 °C for all $PE_{v\text{-insol}}$ materials. Additionally, within the $PE_{v\text{-insol}}$ samples, the rubbery plateau is also apparent, further confirming the network formation within the insoluble fractions. While E' at 150 °C for PE_v materials trended strongly with increasing GPOSS content, where there was a 0.6 MPa increase from 0.5 MPa for PE_v-0.5 to 1.1 MPa for PE_v-3.0, within the $PE_{v\text{-insol}}$ series, the change in storage modulus above T_m was insignificant. Specifically, there was only a slight increase in the plateau modulus, where E' at 150 °C was 2.2, 2.0, 2.2, 2.3, and 2.4 MPa for $PE_{v\text{-insol}}$ samples with ratios of 0.5, 1.0, 1.5, 2.0, and 3.0, respectively. Therefore, the overall increase in plateau modulus in PE_v samples with higher crosslinker content is attributed to the increased gel fraction, rather than changes in the network formation behavior.
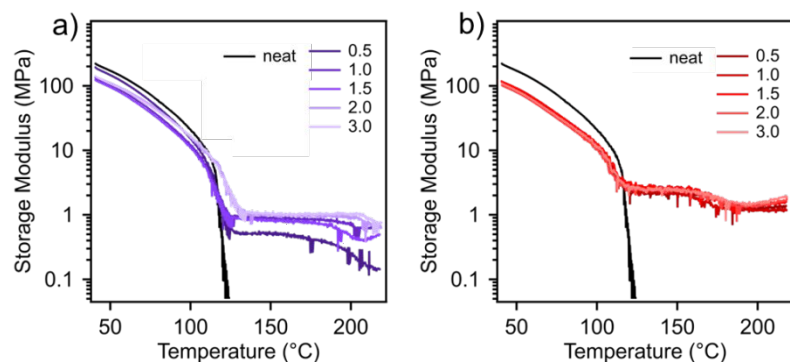

Figure 9. DMA showing the storage modulus over a temperature ramp for (a) PE_{neat} (black) and PEv samples (purple), and (b) PE_{neat} and $PE_{v\text{-insol}}$ samples (red).

To further understand the impact of number of functional groups in crosslinker units, an analogue material using a bifunctional crosslinker, bisphenol A diglycidyl ether (DGEBA) at a 1:1 molar ratio of epoxide groups to MA content, referred to as PE_v-1.0-DGEBA, was compounded. From DMA results, it can be found that PE_v-1.0-DGEBA showed similar E' at 50 °C (104.8 MPa) to the GPOSS crosslinked PE_v-1.0 (104.1 MPa), shown in Figure S17a. $T_{m,onset}$ and $T_{m,endset}$ also fell within the same range of PE_v-1.0 material at 103.4 and 124.3 °C, respectively. However, E' in the rubbery plateau for PE_v-1.0-DGEBA is notably higher at 1.4 MPa compared with the GPOSS at the same reactive moiety ratio, indicative of a higher level of crosslinking within the bifunctional

crosslinker system. This behavior can be explained by the insoluble crosslinked levels observed through the gel fraction tests, where PE$_v$-1.0-DGEBA has the highest gel fraction at 71.5 %, which is 16.4 % higher than PE$_v$-1.0 and 2.7 % higher than PE$_v$-3.0 (Figure S18), confirming more crosslinking within PE$_v$-1.0-DGEBA. The similarity of E' at 50 °C also corresponds with the similar $\chi_{c,PE}$ found through DSC of both PE$_v$-1.0-DGEBA and the PE$_v$ materials, at 42.8 and 45.3 % crystallinity, respectively (Figure S19), suggesting the modulus is more heavily dependent on crystallinity in general. When looking at the PE$_{v\text{-insol}}$-1.0-DGEBA DMA behavior compared with the rest of the PE$_{v\text{-insol}}$ materials, the properties are quite comparable (Figure S17b). Specifically, E' at 50 °C is 85.4 MPa for PE$_{v\text{-insol}}$-1.0-DGEBA, which falls within the previously described range for PE$_{v\text{-insol}}$ materials. T$_{m,onset}$ for the insoluble fraction of the DGEBA vitrimer is also 101.6 °C, within the same range as the GPOSS-based vitrimers. Finally, the plateau modulus for PE$_{v\text{-insol}}$-1.0-DGEBA is very similar to PE$_{v\text{-insol}}$-3.0, a material with similar gel fraction, at 2.4 MPa. Comparisons of the mechanical properties and insoluble fractions between PE$_v$-1.0-DGEBA and other PE$_v$ materials (crosslinked by GPOSS) are presented in Figures S20 and S21. These results indicate that changes in crosslinking identity and content primarily affect the gel fraction rather than the network topology, which in turn influences the mechanical properties of the vitrimers. These behaviors, in addition to the presence of unreacted epoxide groups in PE$_v$ samples (Figure S22) suggest that although GPOSS has eight reactive arms, it is likely that only two were utilized on average.

4. Conclusions

This study investigates the effects of crystallinity, crosslinker identity, and content on the thermal and mechanical properties of PE-derived vitrimers using 8-arm POSS-based crosslinkers. Crosslinking improves strength but decreases stretchability and modulus, as a result of reduced crystallinity and network formation. Analysis of soluble and insoluble fractions shows that crosslinker identity and content primarily affect gel fraction content rather than the network topology of the crosslinked phase. Moreover, despite the presence of eight reactive arms on the GPOSS crosslinker, our results suggest that only two of them might be effectively utilized for even at high stoichiometric ratios, which may be attributed to the low MA reactive group density on PE backbones. This work offers valuable insights into the use of multifunctional crosslinkers in PO-derived vitrimer systems, highlighting how overall material performance can be collectively impacted by crosslink density, gel phase fraction, and polymer crystallinity.

5. Author contributions

Mikaela Sadri: Writing – original draft, Methodology, Investigation. **Andrew Barbour:** Investigation. **Travis L. Thornell:** Writing – review & editing. **J. Kent Newman:** Writing – review & editing. **Zhe Qiang:** Writing – review & editing.

6. Conflicts of interest

There are no conflicts to declare.

7. Data availability

The data supporting this article have been included as part of the Supplementary Information.

9. Notes and references

1   N. J. Van Zee and R. Nicolaÿ, *Prog Polym Sci*, 2020, **104**, 101233.

2   B. M. El-Zaatari, J. S. A. Ishibashi and J. A. Kalow, *Polym Chem*, 2020, **11**, 5339–5345.

3   B. R. Elling and W. R. Dichtel, *ACS Cent Sci*, 2020, **6**, 1488–1496.

4   B. Soman and C. M. Evans, *Soft Matter*, 2021, **17**, 3569–3577.

5   P. Chakma and D. Konkolewicz, *Angewandte Chemie - International Edition*, 2019, **58**, 9682–9695.

6   L. Zhong, Y. Hao, J. Zhang, F. Wei, T. Li, M. Miao and D. Zhang, *Macromolecules*, 2022, **55**, 595–607.

7   J. Luo, X. Zhao, H. Ju, X. Chen, S. Zhao, Z. Demchuk, B. Li, V. Bocharova, J. M. Y. Carrillo, J. K. Keum, S. Xu, A. P. Sokolov, J. Chen and P. F. Cao, *Angewandte Chemie - International Edition*, DOI:10.1002/anie.202310989.

8   J. Joe, J. Shin, Y. S. Choi, J. H. Hwang, S. H. Kim, J. Han, B. Park, W. Lee, S. Park, Y. S. Kim and D. G. Kim, *Advanced Science*, 2021, **8**, 1–11.

9   J. Zheng, Z. M. Png, S. H. Ng, G. X. Tham, E. Ye, S. S. Goh, X. J. Loh and Z. Li, *Materials Today*, 2021, **51**, 586–625.

10   M. Röttger, T. Domenech, R. van der Weegen, A. Breuillac, R. Nicolaÿ and L. Leibler, *Science (1979)*, 2017, **356**, 62–65.

11   R. G. Ricarte, F. Tournilhac and L. Leibler, *Macromolecules*, 2019, **52**, 432–443.

12   B. Soman, K. S. Schweizer and C. M. Evans, *Macromolecules*, 2023, **56**, 166–176.

13   M. O. Saed, X. Lin and E. M. Terentjev, *ACS Appl Mater Interfaces*, 2021, **13**, 42044–42051.

14   T. Debsharma, N. S. Purwanto, L. M. Fenimore, S. Mitchell, J. Kennedy and J. M. Torkelson, *Polym Chem*, 2024, **15**, 2167–2176.

15   J. Huang, Z. Gong and Y. Chen, *Polymer (Guildf)*, 2022, **242**, 124569.

16   S. Ash, R. Sharma, M. Shaker, S. Patil, S. Cheng and M. Rabnawaz, *Polymer (Guildf)*, 2024, **308**, 127374.

17   J. Zhang, X. Li, S. Zhang, W. Zhu, S. Li, Y. Zhang, Y. Hu and G. Zhou, *ACS Appl Polym Mater*, 2023, **5**, 8379–8386.

18   C. A. Tretbar, J. A. Neal and Z. Guan, *J Am Chem Soc*, 2019, **141**, 16595–16599.

19   A. Zych, R. Pinalli, M. Soliman, J. Vachon and E. Dalcanale, *Polymer (Guildf)*, DOI:10.1016/j.polymer.2020.122567.

20   A. Vilanova-Pérez, S. De la Flor, X. Fernández-Francos, À. Serra and A. Roig, *ACS Appl Polym Mater*, 2024, **6**, 3364–3372.

21   Z. He, H. Niu, L. Liu, S. Xie, Z. Hua and Y. Li, *Polymer (Guildf)*, DOI:10.1016/j.polymer.2021.124015.

22   Y. Yang, L. Huang, R. Wu, Z. Niu, W. Fan, Q. Dai, L. Cui, J. He and C. Bai, *ACS Appl Mater Interfaces*, 2022, **14**, 3344–3355.

23   Y. Gao and H. Niu, *Polym Chem*, 2024, **15**, 884–895.

24   G. P. Kar, M. O. Saed and E. M. Terentjev, *J Mater Chem A Mater*, 2020, **8**, 24137–24147.

25   M. Sadri, S. Patil, J. Perkins, Z. Gunter, S. Cheng and Z. Qiang, *ACS Appl Polym Mater*, 2023, **5**, 4056–4068.

26   Y. Xiao, P. Liu, W. J. Wang and B. G. Li, *Macromolecules*, 2021, **54**, 10381–10387.

27   L. W. Hill, *Prog Org Coat*, 1997, **31**, 235–243.

28   L. Matějka, A. Strachota, J. Pleštil, P. Whelan, M. Steinhart and M. Šlouf, *Macromolecules*, 2004, **37**, 9449–9456.

29   M. Tsige and M. J. Stevens, *Macromolecules*, 2004, **37**, 630–637.

30   P. J. Hayes, D. Konkolewicz and M. B. Zanjani, *Phys Rev Mater*, 2022, **6**, 29–37.

31   H. Berk, M. Kaya and A. Cihaner, *Polym Chem*, 2022, **13**, 5152–5158.

32   F. Hajiali and M. Marić, *Journal of Polymer Science*, 2020, **58**, 1503–1520.

33   R. Shivakumar, A. Bolker, S. H. Tsang, N. Atar, R. Verker, I. Gouzman, M. Hala, N. Moshe, A. Jones, E. Grossman, T. K. Minton and E. H. Tong Teo, *Polymer (Guildf)*, 2020, **191**, 122270.

34   J. Zhou, X. Zhang, S. Zhao, C. Ye, Z. Zhang, S. W. Kuo and Z. Xin, *Polymer (Guildf)*, 2022, **244**, 124561.

35   L. Miao, L. Zhan, S. Liao, Y. Li, T. He, S. Yin, L. Wu and H. Qiu, *Macromol Rapid Commun*, 2024, **45**, 1–31.

36   M. X. Nie, J. Wang, Q. Zhang, D. Han and Q. Fu, *J Mater Chem A Mater*, 2024, 24214–24225.

37   C. Li, Y. Zhang and Y. Zhang, *Polym Test*, 2003, **22**, 191–195.

38   L. Yang, F. Zhang, T. Endo and T. Hirotsu, *Macromolecules*, 2003, **36**, 4709–4718.

39   M. C. Montoya-Ospina, H. Verhoogt, M. Ordner, X. Tan and T. A. Osswald, *Polym Eng Sci*, 2022, **62**, 4203–4213.

40   L. M. Fenimore, B. Chen and J. M. Torkelson, *J Mater Chem A Mater*, 2022, **10**, 24726–24745.

41   M. Maaz, A. Riba-Bremerch, C. Guibert, N. J. Van Zee and R. Nicolaÿ, *Macromolecules*, 2021, **54**, 2213–2225.

42   M. Joshi, B. S. Butola, G. Simon and N. Kukaleva, *Macromolecules*, 2006, **39**, 1839–1849.

43   M. J. Hato, S. S. Ray and A. S. Luyt, *Macromol Mater Eng*, 2008, **293**, 752–762.

44   A. Peterlin, *Colloid Polym Sci*, 1987, **265**, 357–382.

45   Y. P. Khanna, E. A. Turi, T. J. Taylor, V. V. Vickroy and R. F. Abbott, *Macromolecules*, 1985, **18**, 1302–1309.

46   I. S. Kolesov, R. Androsch and H.-J. Radusch, *Macromolecules*, 2005, **38**, 445–453.

47   A. Sharif, N. Mohammadi and S. R. Ghaffarian, *J Appl Polym Sci*, 2009, **112**, 3249–3256.

Data Availability Statement

The data supporting this article have been included as part of the Supplementary Information.